

AD-A108 151

HARVARD COLL OBSERVATORY CAMBRIDGE MA
SPECKLE IMAGE RECONSTRUCTION OF SOLAR FEATURES. (U)
MAY 81 R W NOYES, R V STACHNIK, P NISENSEN

F/G 3/2

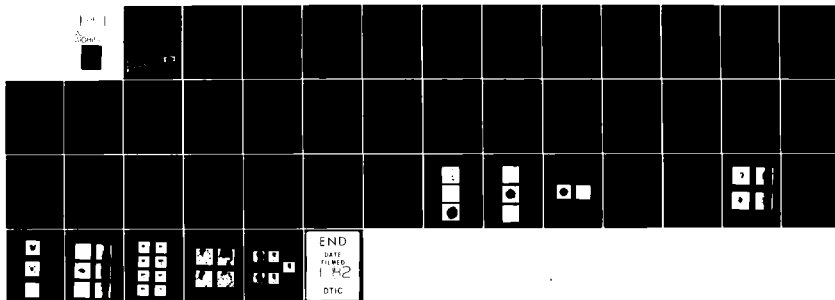
F1962R-78-C-0026

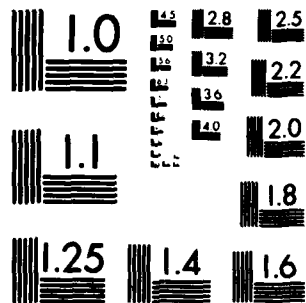
UNCLASSIFIED

AFGL-TR-81-0155

NL

1-1
SOLAR





MICROCOPY RESOLUTION TEST CHART
NATIONAL BUREAU OF STANDARDS-1963-A

AD A108151

Unclassified

SECURITY CLASSIFICATION OF THIS PAGE (When Data Entered)

REPORT DOCUMENTATION PAGE		READ INSTRUCTIONS BEFORE COMPLETING FORM
1. REPORT NUMBER AFGL-TR-81-0155	2. GOVT ACCESSION NO. AD-A108251	3. RECIPIENT'S CATALOG NUMBER
4. TITLE (and Subtitle) SPECKLE IMAGE RECONSTRUCTION OF SOLAR FEATURES		5. TYPE OF REPORT & PERIOD COVERED Final Report 24 Feb 78 - 24 Feb 81
		6. PERFORMING ORG. REPORT NUMBER
7. AUTHOR(s) R. W. Noyes R. V. Stachnik P. Nisenson		8. CONTRACT OR GRANT NUMBER(s) F19628-78-C-0026
9. PERFORMING ORGANIZATION NAME AND ADDRESS Harvard College Observatory 60 Garden Street Cambridge, MA 02138		10. PROGRAM ELEMENT, PROJECT, TASK AREA & WORK UNIT NUMBERS 61101F 2311G3AI
11. CONTROLLING OFFICE NAME AND ADDRESS Air Force Geophysics Laboratory Hanscom AFB, Massachusetts 01731 Monitor/Richard Radick/PHS		12. REPORT DATE 15 May 81
14. MONITORING AGENCY NAME & ADDRESS (if different from Controlling Office)		13. NUMBER OF PAGES 44
		15. SECURITY CLASS. (of this report) Unclassified
		15a. DECLASSIFICATION/DOWNGRADING SCHEDULE
16. DISTRIBUTION STATEMENT (of this Report) Approved for public release; distribution unlimited		
17. DISTRIBUTION STATEMENT (of the abstract entered in Block 20, if different from Report)		
18. SUPPLEMENTARY NOTES		
19. KEY WORDS (Continue on reverse side if necessary and identify by block number) Speckle Interferometry, Speckle Imaging, Solar Imaging		
20. ABSTRACT (Continue on reverse side if necessary and identify by block number) The hardware and software required to demonstrate and evaluate the speckle imaging process for use on solar features have been developed and tested. A video speckle camera has been designed, constructed, and successfully used to record data for a wide variety of astronomical objects, including solar features. The problems associated with recovering images from speckle data have been explored extensively. Particular attention has been given to identifying and correcting effects due to noise bias and edges in images reconstructed from real as well as simulated data. The principles involved in imaging solar features at improved		

DD FORM 1 JAN 73 1473

Unclassified 110432
SECURITY CLASSIFICATION OF THIS PAGE (When Data Entered)

Unclassified

SECURITY CLASSIFICATION OF THIS PAGE(When Data Entered)

20. Abstract (cont.)

— resolution by means of speckle techniques have been delineated, and sample images recovered from a variety of test data.

Unclassified

SECURITY CLASSIFICATION OF THIS PAGE(When Data Entered)

TABLE OF CONTENTS

I.	Introduction	4
II.	Technical Background	4
III.	Description of Current Hardware	9
IV.	Major Program Accomplishments	14
V.	Discussion of Project Results	16
VI.	Conclusions	23
References		25
Figures		26

Accession For	
NTS GRA&I	<input checked="checked" type="checkbox"/>
DTIC TAB	<input checked="checked" type="checkbox"/>
Unannounced	<input type="checkbox"/>
Justification	
Re	
Distribution/	
Availability Codes	
Avail and/or	
Special	

A

I. Introduction

The purpose of this effort was to develop the hardware and software required to demonstrate and evaluate the speckle imaging process for use on solar features. Speckle imaging is a procedure for recovering high-resolution images from large telescopes, despite the degrading effect of the Earth's atmosphere. At typical large telescopes, the diffraction resolution limit, which may be reached with speckle processing, is a factor of between 10 and 50 finer than the one arcsecond limit typical of seeing.

The program entailed algorithm development, characterization and testing of hardware, characterization of the procedure itself, and gathering, processing and analysis of data.

An important goal was implementation of procedures for processing of solar data. Laboratory and on-telescope experiments have demonstrated that the special problems that arise in this case are tractable and successful reconstructions have been produced.

II. Technical Background

a. Overview

Speckle imaging is a technique for recovering diffraction-limited resolution from atmospherically degraded images recorded at the focus of a large telescope. The technique evolved from speckle interferometry, a process that has been well demonstrated and which has produced many astronomically significant results. However, in speckle interferometry, only image autocorrelations are obtained from the process, while in speckle imaging, true diffraction-limited images can be reconstructed. In both processes, a series of short-exposure, highly magnified images are recorded, allowing sufficient time between exposures so that the atmosphere is decorrelated from frame to frame. In speckle interferometry, the recorded images are Fourier transformed and then the individual spatial power spectra are summed.

This procedure is equivalent to summing the autocorrelations of the speckle images. The process has been demonstrated to yield diffraction-limited results with the signal-to-noise ratio proportional to the square root of the number of frames integrated and to be highly insensitive to telescope aberrations. In speckle imaging, the averaging process is nearly identical with the interferometry process except that the phase in each Fourier transform is encoded in such a way that after averaging, both the object amplitude and phase can be recovered and true diffraction-limited images reconstructed. The key to the phase recovery process is the recognition, first made by Knox and Thompson (1974), that, while the transform phase averaged at any point yields a result characteristic of the very large fluctuations due to the atmosphere (the phase at any point is essentially random in the interval zero to 2π), the differences in transform phase between very closely adjacent points in the spatial frequency plane can be quite small (fractions of a radian) and arrays of transform phase differences will sum to values characteristic of the diffraction-limited object.

In our current implementation, the imagery is recorded at the telescope with a highly developed video recording system capable of operation over a very large range of light levels using a reliable analog mass storage medium—videotape. The images are then digitized and processed in the laboratory.

b. Image Processing Procedure

The image processing procedure is shown schematically in Figure 1. Quantities inside boxes represent data arrays.

Each image $I(\vec{x})$ is Fourier transformed to obtain $I(\vec{\omega})$

$$I(\vec{\omega}) = \int d\vec{x} I(\vec{x}) e^{-i\vec{\omega} \cdot \vec{x}} = A(\vec{\omega}) e^{i\phi(\vec{\omega})} \quad (1)$$

where $\vec{\omega}$ is the frequency space vector, $A(\vec{\omega})$ is the modulus (amplitude) of the transform and $\phi(\vec{\omega})$ is the phase in the transform. A linear phase correction, based

on a calculation in the image plane of the center of mass, is applied to each transform. This correction has an effect on the transform equivalent to an operation in image space which moves each image to a common center. From each transform we generate four saved arrays each of which is averaged with the results obtained from the transforms of the previous images. These arrays represent:

$$\langle I(\vec{\omega}) \rangle = \langle A(\vec{\omega}) e^{i\phi(\vec{\omega})} \rangle \quad (2)$$

$$\langle |I(\vec{\omega})|^2 \rangle = \langle |A(\vec{\omega})|^2 \rangle \quad (3)$$

$$\langle I^*(\vec{\omega}) I(\vec{\omega} + \Delta\vec{\omega}_x) \rangle = \langle A(\vec{\omega}) A(\vec{\omega} + \Delta\vec{\omega}_x) e^{i[\phi(\vec{\omega} + \Delta\vec{\omega}_x) - \phi(\vec{\omega})]} \rangle \quad (4)$$

$$\langle I^*(\vec{\omega}) I(\vec{\omega} + \Delta\vec{\omega}_y) \rangle = \langle A(\vec{\omega}) A(\vec{\omega} + \Delta\vec{\omega}_y) e^{i[\phi(\vec{\omega} + \Delta\vec{\omega}_y) - \phi(\vec{\omega})]} \rangle \quad (5)$$

where $\langle \rangle$ indicates the ensemble average and $*$ is the complex conjugate.

The quantity in Eq. (2) is equivalent to the transform of the direct sum of the images and is used to reweight the low frequency amplitudes in the transfer function. Equation (3) gives the usual result of speckle interferometry, the power spectrum, and is used for the amplitude estimates. Equations (4) and (5) effectively yield phase differences between adjacent points in frequency space and are the quantities from which the transform phases are extracted. $\Delta\omega_x$ and $\Delta\omega_y$ are chosen small enough to ensure that the phases in Eqs. (4) and (5) never exceed the range of $\pm \pi/2$. $\Delta\omega_x$ is normally set equal to $\Delta\omega_y$ and the image scale is adjusted so that they are both one sample spacing in Fourier space. This implies that the atmospheric seeing disk diameter is adjusted to be less than half the full image field diameter. After averaging, the phase differences obtained from Eqs. (4) and (5) must be integrated to yield the transform phases. This is done using an iterative least squares fitting routine which distributes the residual errors due

to incomplete averaging over the entire transform plane. The procedure takes account of amplitude variations in phase space and weights most heavily those paths which are best known. This approach has been successfully applied to the problem of extracting phases in shearing interferograms in active optics applications (Hardy, Lefebvre and Kolopoliou, 1977). The amplitudes used in the reconstruction $A_r(\vec{\omega})$ are given by

$$A_r(\vec{\omega}) = [\langle |A(\vec{\omega})|^2 \rangle - \delta \cdot |\langle A(\vec{\omega}) e^{i\phi(\vec{\omega})} \rangle|]^{\frac{1}{2}}$$

Here δ is a constant which is proportional to the number of speckles in the seeing disk. This approach is motivated by the derivation of the speckle transfer function by Korff (1973) and Dainty (1974). Finally, the calculated phases are combined with the reweighted amplitudes $A_r(\omega)$ and Fourier transformed to obtain the reconstructed image.

One other important operation is compensation for the effects of photon noise on the transform. Single photon correlations introduce frequency-dependent biases to the amplitudes and add frequency-dependent complex biases to the phase differences. When light levels are sufficiently low so that the effect of photon noise can no longer be neglected, Eqs. (3), (4) and (5) become

$$\langle |I(\vec{\omega})|^2 \rangle = (|\bar{N}R(\vec{\omega})|^2 \langle |A(\vec{\omega})|^2 \rangle + \bar{N}R(\vec{\omega}) |\langle A(0) e^{i\phi(0)} \rangle| \quad (6)$$

$$\langle I^*(\vec{\omega}) I(\vec{\omega} + \Delta\vec{\omega}_x) \rangle = \quad (7)$$

$$(|\bar{N}R(\vec{\omega})|^2 \langle A(\vec{\omega}) A(\vec{\omega} + \Delta\vec{\omega}_x) e^{i[\phi(\vec{\omega} + \Delta\vec{\omega}_x) - \phi(\vec{\omega})]} \rangle + \bar{N}R(\vec{\omega}) |\langle A(\Delta\vec{\omega}_x) e^{i\phi(\Delta\vec{\omega}_x)} \rangle|$$

$$\langle i^*(\vec{\omega}) i(\vec{\omega} + \Delta\vec{\omega}_y) \rangle =$$

(8)

$$(|\bar{N}R(\vec{\omega})|)^2 \langle A(\vec{\omega}) A(\vec{\omega} + \Delta\vec{\omega}_y) e^{i[\phi(\vec{\omega} + \Delta\vec{\omega}_y) - \phi(\vec{\omega})]} \rangle + \bar{N}R(\vec{\omega}) \langle A(\Delta\vec{\omega}_y) e^{i\phi(\Delta\vec{\omega}_y)} \rangle$$

The bias terms in (6), (7), and (8) are all measurable from the direct sum and are proportional to N , the number of photons in each frame, or, in the ensemble averages, to the total number of photons N . The frequency dependence is determined empirically from the observed photon "shape," corresponding to the detector response function, and is represented by $R(\vec{\omega})$. The bias effects are removed by subtracting appropriately-scaled functions from the amplitude and phase difference arrays.

The image recovery procedure is, then, summarized as follows:

- Image fourier transformation
- Fourier transform phase difference coding
- Summation of the coded transforms
- Application of phase reconstruction algorithm
- Compensation for phase and amplitude noise bias terms
- Application of amplitude reweighting
- Transformation back to image space
- Image display.

Actual implementation of the required programs was carried out on a number of computers in succession. Initially, this included the AFGL CDC 6600 in Bedford, for which remote operation proved extremely difficult and turn-around was very slow and the SAO CDC 6400, which facility was closed down not long after our programs became operational. Much of the development work was done on a Nova 1200 which had the advantage of being a dedicated machine with good display capabil-

ity, but which had limited core space. For manipulation of larger arrays, we moved to the new SAO VAX. For image processing program development, considerable computing power, rapid turn-around and good display capabilities are all highly desirable, and no single facility available to us had all these characteristics. Although the difficulties imposed by the moves were very considerable and time consuming, and the mix of computers we are now using is reasonably efficient.

III. Description of Current Hardware

Early speckle imaging experiments done with film were severely hampered by the noisy and cumbersome nature of that recording medium. In addition to the fact that recorded data could not be inspected at the telescope, digitization was a slow and laborious process and film grain effects were difficult to calibrate and compensate. The electronic system developed for the project is far more efficient and simple to use.

An electronic speckle data recording system must be able to record spectrally filtered, short exposure images at high magnification. Because the exposures must be short enough to "freeze" the seeing, and the magnification high enough to record diffraction-limited image structure, exposure levels are low even for bright objects and high detector gain is required. In addition, compensation for atmospheric dispersion must be made, and the detector should have no "memory" of earlier recorded images (no "lag"). Ideally, the camera would be able to record large numbers of images and have a high duty cycle.

A diagram of the electronic speckle camera that we have developed is shown in Figure 2.

The on-telescope recording apparatus is relatively simple, light-weight and reliable. The basic detector is an ISIT video camera which can, if desired, be lens-coupled to an additional stage of high-gain intensification to insure detectability of individual photons. This design has the advantage of being useful over the widest

possible range of light levels. As an aid to field finding, a three path optical system permits direct viewing of the image, low magnification video display, and high magnification video display, also used for data recording. A filter mount holds up to six interference filters, as well as prisms to redirect the beam to either the optical or video low magnification path.

The video images are recorded on a standard video tape recorder with one (1/60th second) video field in eight containing a useful image. The sequence is as follows:

Field 1: Rotating chopper wheel synchronized to camera exposes photocathode for 4-16 ms, adjustable with the seeing change time. During this interval, the camera read-out beam is switched off, using blanking control.

Field 2: Read-out beam is turned on and the vidicon silicon surface is read out normally.

Field 3: A light emitting diode flashes, saturating the silicon surface in the camera to insure that the entire photocathode is erased uniformly, leaving no residual image.

Fields 4, 5, 6, 7, 8: Normal read-out to discharge camera silicon surface.

All fields are recorded and Field 2, containing the desired image, is marked for subsequent digitization by means of a tone on the audio track of the video recorder. This procedure is depicted schematically in Figure 3.

It is worth elaborating on a few design features of the camera, the importance of which were underscored in early tests. The most significant of these features is the light-emitting diode "flasher" used to eliminate the lag problem. Our choice of an ISIT sensor was dictated by the fact that we wished to be able to operate over a very large range of light levels, including the photon starvation regime. Solid state sensors, such as CCDs, do not suffer as severely from lag as do video sensors, but we did not regard the requisite intensified CCD technology to be

sufficiently highly developed. We still feel this to be true.

The response of a camera like the ISIT to a localized light impulse over a series of readout fields is rapid erasure in the first ten fields, followed by a long "tail," during which little erasure occurs, and a pedestal builds up. The pedestal distribution is that of the coarse object structure and the effect of this pedestal is both to diminish the contrast of high frequency detail and, at low light levels, to make level slicing, for photon detection, more difficult. The synchronized flasher eliminates the problem.

A second important design feature is the presence of the microchannel plate intensifier which insures detection of photons at very high signal-to-noise at the lowest light levels. This high gain makes photon counting operations possible.

Digitization of the analog video-taped images is performed in the laboratory using a system designed and built in-house. We feel that post-recording digitization increases the reliability of the system as a whole. On-telescope digitization is possible with the existing apparatus and will become more attractive when facilities for real-time data processing become available. Without real-time processing, meaning the ability to perform $(128)^2$ 2-D FFTS at a rate of 7.5 per second, on-telescope digitization would mean generation of 2400 ft tapes of digitized images at a rate of one every 4 minutes. Analog format storage is clearly more efficient. A one-hour videotape holds 2×10^5 images.

The video images initially have a resolution of about 300×400 elements. Electrical filtering in one direction, and weighted averaging of three digitized lines in the other, are used to produce 128×128 8-bit digitized arrays for each recorded frame. 8 K of computer memory is used as a buffer, and the arrays are transferred from this buffer to computer tape via a 125 ips, 1600 bpi drive. (It is the speed of this drive as well as the erasure requirements of the camera's silicon surface that established the 1 part in 8 duty cycle.) Hardware logic is used to

pick off the required line and frame synchronization pulses, and to manage timing and frame counting.

The decision to go to in-house design and construction of the digitizer was important since very severe vendor performance problems were encountered under the original approach.

By means of a simple optical system we have been able to produce speckle patterns in the laboratory that precisely match what is produced atmospherically at various telescopes. The speckle can be frozen or can be made to vary temporally on a time scale that is identical to what is observed at various telescopes. This allows us to form in the laboratory "atmospherically degraded" images of various objects such as point sources, binary stars, extended objects, etc., at various light levels thus allowing a complete test of the entire speckle process that reconstructs a diffraction limited image.

A block diagram of the optical system is shown in Fig. 4. It can easily be shown that the dimensions (in mm) of a diffraction limited image of a point source depend only on the f number of the image and the wavelength of light. This means we can form with a small lens a diffraction-limited image that is identical in all respects to one formed by a large telescope.

In order to simulate the wavefront distortions that are caused by the atmosphere, a demagnified image of the entrance pupil is formed by optical system A such that its diameter is about 10-15 times the correlation length of a diffusing screen. In the process of demagnifying the entrance pupil, the image under study is magnified. Optical system B, essentially a mirror image of system A, remagnifies the pupil and demagnifies the image under study. The net result is an "atmospherically degraded" image with about 10-15 speckles across the image of a point source (equivalent to a 1.5-meter telescope with 1 arcsecond "seeing"). The temporal behavior is added simply by moving the diffusing screen linearly with a motor.

The optical system can be easily changed to match the f number of any telescope and optical systems A and B can be changed to match any atmospheric seeing conditions. All in all, the apparatus gives a realistic and readily controllable simulation.

IV. Major Program Accomplishments

Under Air Force support, and with parallel NASA funding, we have been able to achieve the following milestones in the speckle imaging program:

- Construction of laboratory apparatus for realistic simulation of imaging through a turbulent medium.
- Construction of an image-intensified film camera.
- Extensive laboratory studies using the film system.
- Observing runs using the film system.
- Image reconstruction of simple targets (binary stars), using the film system, which show 0.05 arcsecond resolution.
- Numerical experiments demonstrating high-resolution image reconstruction of complex targets.
- Low resolution (factor of 2-3 improvement) reconstructions from film-recorded images of complex solar features (limited signal-to-noise ratio was present in input digitized images).
- Construction of video recording system.
- Construction of video image digitization system.
- Laboratory studies using video system.
- Observing runs using video system.
- Installation of hardware and software for photon counting operation.
- Development of extensive digital image display capability.
- Reconstruction of solar features from video data. Factor of 4 improvement despite noise and lag effects.
- Study of image plane apodization to reduce edge effects.

- Investigation of video lags and installation of optical "flasher" to insure uniform erasure.
- Substantial noise reduction modifications to video camera.
- Investigation of effects of very large phase fluctuations.
- Solution of amplitude reweighting and photon noise bias problems.
- Very low light level simulations.
- Implementation of programs on dedicated Nova 1200 and PDP 11/34 computers.
- Reconstruction of complex objects recorded with the video system in the laboratory.

V. Discussion of Project Results

The major technical subdivisions of this project included software development, hardware development, and process evaluation and testing, which, in many cases, combined the hardware and software assessment tasks. Work in this last area began as soon as the algorithms were working and represented the major part of our effort. It was our experience that many details of the data taking and processing procedure interacted in sufficiently subtle ways that the testing process benefitted greatly from the presence of a laboratory testbed for the system. Processing actual data proved much more difficult than the computer simulations alone would have led us to believe. The following discussion summarizes some important experiments in our testing program.

Much of our testing program was based on observation of binary stars. The reconstructions and various intermediate results are particularly easy to interpret for these simple sources and edge, noise bias and reweighting problems can be minimized. True extended objects are much more difficult. The additional information provided by full image processing over conventional autocorrelation or power spectrum speckle processing of binary stars is not great, but the information can be useful and experience gained in processing these sources has been substantial.

Our first successful reconstruction of an astronomical object was Capella, a nearly equal magnitude 0.05 arcsecond binary. The data used were some old film recorded images obtained by one of us at the 5-Meter Hale telescope as part of the original speckle interferometry experiments. The eighteen images available were digitized at the Yale PDS microdensitometer and processed as 64 x 64 arrays. Because of the small array size our field was only 0.8 arcseconds in diameter and the seeing disk greatly overfills the digitized area. Because of the way in which the phase averaging is done, the fluctuations in time of the point-to-point phase differences must be in the range $\pi/2$ to $-\pi/2$ for successful phase

recovery. This is equivalent to saying that the seeing disk must be smaller than one half the field diameter. Our solution to this problem was to multiply the input images by a Gaussian mask. Figure 5 shows an input image ,a, (no mask), a reconstruction from the Gaussian-masked data, b, and an attempt at reconstruction without the mask, c. Despite the relatively poor quality of the data, and the limited number of frames, the reconstruction is reasonably good, although a few small artifacts are present.

Figure 6 was an early test of the video system, in which a laboratory-simulated double star was reconstructed. Here, the input object was an unequal magnitude binary for which the optical system, in the absence of seeing, produced slightly comatic images (a). b is a recentered direct sum of the seeing-degraded images and c is a reconstruction from 100 frames. The reconstruction preserved the relative magnitude of the two stars and verified that there were no unexpected problems with the video system. The reconstruction also shows nicely the relative insensitivity of the process to telescope aberrations, a characteristic also typical of speckle interferometry. Note that figure 15 demonstrates aberration insensitivity for more complex sources.

The foregoing reconstructions demonstrated our ability to recover images from film-recorded on-telescope data and video-recorded lab data. A staple of our video system observing runs has been binary stars, recorded largely for characterization purposes. These observations are useful not only for process and camera testing but for measuring factors, such as correlation time, correlation distance and isoplanatism, associated with the atmosphere. Figure 7 is a continuous tone representation of the direct sum and recovered images of the 0.17 arcsecond binary ADS11460A and figure 8 is a 3-D plot of the 0.53 arcsecond binary ADS14073, again showing both sum and reconstruction. Figure 8b, demonstrates how clean the reconstructions can be for, in this case, only a few hundred frames. It should be

noted that the direct sums are produced from individually recentered images and are thus considerably better than an ordinary photograph or other direct image integration.

Early computer simulations of complex object recovery were very encouraging. Figure 9 shows an experiment in which the greek letter gamma and a point were convolved with 100 film recorded speckle images of a sixth magnitude star. The star images were recorded at a 2.1 meter telescope. a,b,c,d,e and f are, respectively, the input object, the diffraction-limited input object, a sample star image, a single object-star convolution, a direct sum of 100 object-star convolutions and a reconstruction. Except for the absence of sensor-related noise, this is an impressive simulation. In fact, noise, including fixed pattern noise, digitizer noise, shot noise and photon noise, is a serious problem for the case of actual reconstructions.

At very high contrast levels and for the low noise case, simulations performed with the video system have been nearly as impressive as the computer simulations. The object, in this instance, is a simulated asteroid having an irregular shape and two high contrast surface features. 10a shows the object through the simulator when the seeing phase plate is removed from the telescope pupil (the plate is replaced by a clear piece of glass to preserve the optical characteristics of the system). 10b shows the same source when the phase plate is re-inserted, and 10c is the result of direct summation of 100 short exposure images like 10b. 10d is the result of processing the same 100 frames using the reconstruction procedure.

The subject of photon noise bias compensation was addressed in the Technical Background section. Simulations in which the input frames were degraded by poisson noise were processed using the noise bias compensation procedure with good results. An estimate of the correction to the recovered amplitude and phase difference arrays was made by measuring the amount of power present in the spectrum in an annular region in frequency space just beyond the diffraction

cutoff. Figure 11 is a demonstration of the procedure.

11a is an input source, consisting of a double Gaussian. 11b is single frame of test data generated by convolving the double Gaussian with a film-recorded star image and degrading the result by introducing Poisson-distributed noise corresponding to a noise level of 3000 photons per frame and 11c is an attempt to recover an image from 100 degraded frames without the use of bias compensation. 11d is the image recovered with bias compensation. As with the recovered gamma, the computer simulation was very encouraging. Although noise was present, it was very well behaved, however, in the sense that we were simulating photon noise as unit impulses.

Another experiment demonstrated that, for well behaved noise, bias compensation works down to extremely low light levels. Figure 12a is an image, recorded with the video system, of a checkerboard at an illumination level corresponding to an average of 27 photons per frame. Simple, level-slicing photon detection was invoked in the software. Direct summation of 100 frames yields image b. At this very low light level a prohibitively large number of frames would be required to recover a seeing degraded image. However, a much simpler test was possible. Without bias compensation, processing photon noisy frames with or without seeing present results in a reconstruction consisting of a point. This is evident in figure 11c. The bias-corrected image 12c, however, shows the checkerboard clearly, with no suggestion of a central spike.

Clearly, it is important to verify that real noise, characteristic of our non-photon-counting (but photon-detecting) sensor could be compensated. Figure 13 demonstrates that this is the case. The test was conducted using the simulator with a triple star as the test object. For small values of the bias, given here in arbitrary units that scale with the number of photons per frame, the reconstruction is a point. Even for bias estimates corresponding to errors of only 20% in the

number of photons (bias=20), very significant degradation in the recovered image is evident. With the correct choice of bias value, however, the reconstruction is quite accurate. With the early and rather poor model for mean photon shape used here, residual bias compensation errors lead to the noise spike at upper right. With better models, the spike disappears.

A separate problem arises for objects which have a large angular extent compared to the processed area. The area one can process is limited by either of two considerations: maintenance of isoplanatism over the field and computational or instrumental limitations on the size of the image array. The former concern generally sets the limit at the smaller telescopes commonly used in solar work while, with our array sizes of 64 to 128 elements square, the latter is often the limit at large telescopes. Since many types of objects, the sun in particular, are far larger than our field, we have investigated the problems associated with looking at a small part of an extended object. Figure 14 shows the results of some of these experiments.

In Figure 14, a small portion of a slide of a sunspot group was processed in an effort to better understand the bordering problems. The area we looked at included three small spots and, for ease of computation, the arrays were 64x64 in size. The simulation deals exclusively with the high light level case.

Figure 14a is the diffraction limited image without seeing, and 14b is a 100 frame reconstruction produced with no border in the image plane. 14c is a single short exposure image typical of those from which the reconstruction was produced. Because we have masked the object at the source, above the "atmosphere", the situation to this point is no different from that of the asteroid reconstruction. When all but the central 32x32 elements of each digitized image are zeroed, the effect is to produce a black border in the image plane, and the result of attempting a reconstruction from 100 such frames is shown in 14d. The reconstruction is quite poor and dominated by border effects. This is not surprising, since the image

recovery procedure works by performing an average that emphasises subtle features that repeat, at the expense of atmospheric contributions, which do not. In this case, the border is the dominant constant contribution to the image structure. The reconstruction improves somewhat if an effort is made to center the image within the border in an attempt to minimize motion of image structure across the boundary.

This raises the question of the effects of fixed pattern noise, arising in the sensor system, on the reconstruction. For very extended objects in poor seeing, where sensor structure is most obvious and image structure is least evident, this could be a severe problem. Figure 14e is an unbordered reconstruction in which a fixed 3x3 element black spot was introduced into each input image. The degradation is considerable and substantial artifacts are present.

The last three reconstructions show attempts to minimize the border effects by image plane apodization. An effort, not shown, to use a very slowly-varying ("soft") apodization function - a gaussian - was no more successful than the very hard-edged black border. Intermediate choices were more promising. Apodization functions which soften only at the very edge are shown in 14f and 14g. The shape of the border for 14g is a super-ellipse (of power 8) with a soft edge. This seems more successful than 14f, which used a square border shape. 14h is the same as 14g except that no effort was made to center the images, yet it still yields an acceptable reconstruction.

A clearer impression of the quality of a restored image of an extended source comes from figure 15. Here, the input object is a slide of solar granulation from the Stratoscope project. Like all granulation photographs, the contrast in the available slide was greatly increased over the likely contrast on the actual solar surface. In addition, the gray scale display used to produce the figure rezeroes and renormalizes the images to produce an intensity range greater than the film response range.

Figure 15a is a direct image of the input slide recorded using the video camera and with the seeing plate replaced by a transparent compensator plate. Because the compensator plate was a bit too thin, the scale of the direct image is about 10% smaller than the scale of any of the other images. Figure 15b is a single frame taken with the seeing plate in position, c is a 200 frame direct sum and d is a reconstruction. More detail is evident in the short exposure image (b) than in the direct sum (c) but many of the features are spurious. It is clear that many features seen in d are not present in either b or c. Note that the compensator plate thickness error means that the input speckle frames are necessarily out of focus, yet the reconstruction is quite insensitive to this fact.

Figure 16 is a reconstruction produced from some film data provided us by Dr.S.P.Worden, showing a CaK+ solar feature. The scale across the image is approximately 5 arcseconds. Figure 16a is a single input image, rather noisy, and 16b is the direct sum of the 80 available frames. Figure 16c and 16d are reconstructions from independent 30 frame subsets of the data from which it is possible to gauge which features are likely to be real. Figure 16e is a reconstruction from the full 60 frames. It appears that the 60 frame reconstruction has an improvement in resolution of approximately a factor of three to four over a single frame.

VI. Conclusions

Under this contract, we have designed, constructed and tested a video data recording and digitization system and an atmospheric-imaging simulator. In addition, we have extensively modified, and have tested and characterized, Knox-Thompson image reconstruction programs for the purpose of solar image reconstruction. Both laboratory and on-telescope data have been recorded and processed, yielding successful reconstructions. The most impressive gains in resolution have been accomplished for simple, high contrast objects, such as binary stars. Here, the resolution gains over the seeing limit have been of the order of a factor of 50. For complex objects, having more modest internal contrasts, we have achieved resolution improvements of factors of 4 to 6 and appropriate use of image plane apodization has reduced the edge effect problem. It is unlikely that we have yet found the best practical apodization function, so it appears that the influence of edge effects can be reduced still further.

Variations of exposure during the erase cycle, corresponding to local variations in "pedestal" height, as well as sensitivity variations over the vidicon/intensifier combination, contribute to fixed pattern noise, some component of which is likely to be gain-variable. This is not a problem for reconstruction of relatively contrasting objects of limited extent. For the lower contrast extended objects with which we often deal, however, the presence of a fixed pattern can present serious difficulties since the reconstruction process works by recovering weak spatial distributions which repeat in all the frames. Because reconstructions obtained from actual data sets have been impressive only for high contrast features, we believe that the principal limitation at present is the sensor. Multiplicative flat field correction will certainly help and, because the flash saturation procedure may not produce a uniform background, pedestal subtraction may also be useful. The more severe demands placed on the sensor by solar surface imaging (compared to "detached

object" imaging) lead us to believe that a combination of better uniformity correction of the present sensor (best suited to narrow band imaging-including production of dopplergrams and magnetograms) and acquisition of a new high light level sensor would make the processing far more tractable than it is at present. We believe that the basic principles for recovery of high resolution solar images are well established.

REFERENCES

Harvey, J.W., Lefebvre, J.E., and Koilopolis, C.L., 1977, *J.O.S.A.*, **67**, 360.

Harvey, J.W. and Breckinridge, J.B., 1973, *Ap. J.*, **182**, L137.

Knox, K., and Thompson, B.J., 1975, *Ap. J.*, **193**, L45.

Stachnik, R.V., Nisenson, P., Ehn, D.C., Hudgin, R.H., and Schirf, V.E., 1977, *Nature*,
266, 149.

FIGURES

1. Flow chart illustrating the speckle image reconstruction procedure. Boxes indicate arrays.

2. Diagram of the speckle camera and of the video data digitizer.

3. Video camera timing diagram. The video camera generates the standard 60 fields per second of which one in eight contains useful data. The resulting 7.5 field per second rate is the speed at which the digitizer can operate. During a sequence, field 1 is used for exposure, 2 is read-out, 3 is silicon surface saturation, by means of a pulsed l.e.d., for the purpose of eliminating "memory" of previous fields and fields 4 to 8 are erasure of the silicon surface.

4. Optical diagram of the laboratory speckle simulator. A and B are lens packages. The reduced image of the entrance pupil is scaled to the correlation distance typical of the diffusing screen. The diffusing screen is a piece of ground glass polished on one side.

5. Capella reconstruction. a is single film recorded image of Capella taken at the 5-Meter telescope. The field is approximately 0.6 arcseconds and a Gaussian mask has been used since the seeing disk would otherwise overfill the aperture. b is an eighteen frame reconstruction. c is a reconstruction attempted without the mask. The reconstruction falls because the point-to-point phase fluctuations become too large.

6. Demonstration of aberration insensitivity. a is the double point input object recorded with the video camera and simulator. Note that substantial coma is evident. b is a single frame recorded with the seeing plate in place. c is a 100 frame reconstruction showing little coma.

7. Reconstruction of the binary star ADS11460A. The measured separation of the components is 0.15 arcsecond.

8. Reconstruction of the binary star ADS14073. The 3-D plots demonstrate how clean a reconstruction can be obtained from 200 frames.

9. Computer simulation of image recovery for a complex object (a greek "gamma"). a is the input object, b is the object degraded to diffraction-limited resolution, c is a sample point spread function (a film-recorded stellar image), d is a single object-star convolution, e is a direct sum of 100 frames like d and f is a 100 frame reconstruction. Here, the input images were computer-generated by convolution.

10. Recovery of a laboratory-recorded complex object. a is an image of the object with no seeing, b is a single frame of the object with the seeing plate in place, c is a 100 frame direct sum of the images and d is a 100 frame reconstruction.

11. Computer simulation of photon noise bias compensation. a is the input object, a double Gaussian, b is a single computer-generated atmosphere and photon-noise degraded input frame (3000 photons), c is a reconstruction attempted without compensation for photon noise and d is a reconstruction with photon noise compensation.

12. Demonstration of very low photon level bias compensation. a is a single video-recorded image of a checkerboard at a photon level of 27 per frame. For comparison, b is an image at 2700 photons per frame. Processing 100 images without photon bias compensation would yield a single point. c is the image recovered with compensation, indicating that the process works well even at these very low light levels.

13. Video simulation demonstration of photon noise bias compensation. The first two images are of the input object, a "triple star", with and without the seeing plate. Subsequent images are the reconstructions obtained with different values of the bias parameter, a measure of the number of photons per frame.

14. Demonstration of the need for image plane apodization in reconstructing extended objects. a is the input object and b is a 100 frame reconstruction with no apodization. c is a single short exposure image and d is a reconstruction obtained with a hard edge border. e is a reconstruction attempted for data with a single fixed spot in each input frame. f and g are reconstructions from soft-edge apodized data using square and rounded window shapes, respectively. h is the same as g except that no image recentering was attempted.

15. Reconstruction of an extended field Stratoscope granulation image. a is the input object and b and c are a single frame and a direct sum of 100 frames, respectively. A slight error in compensator plate thickness has introduced a 10% scale difference. d is a 100 frame reconstruction.

16. Reconstruction of a CaK image of the solar surface. The field is approximately 5 arc seconds. a is a single input image a b is a 60 frame direct sum. c and d are independent 30 frame reconstructions and e is a reconstruction from the full 60 frames.

SPECKLE IMAGE RECONSTRUCTION

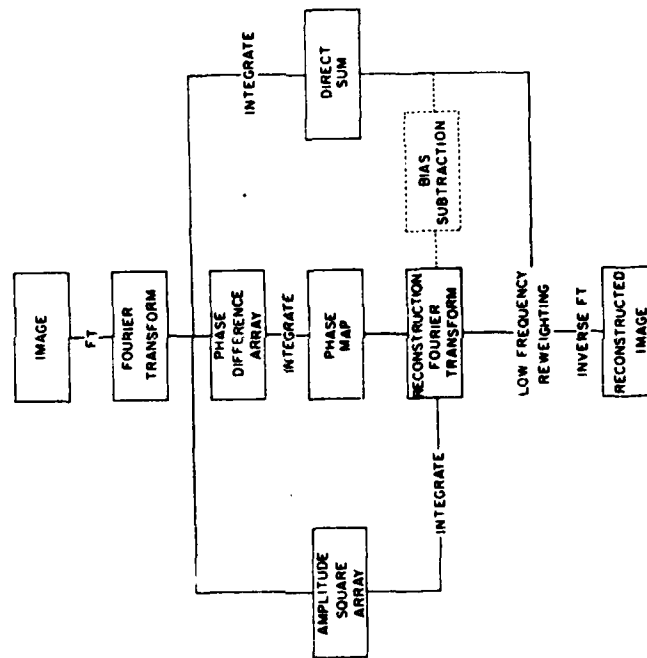


Fig. 1

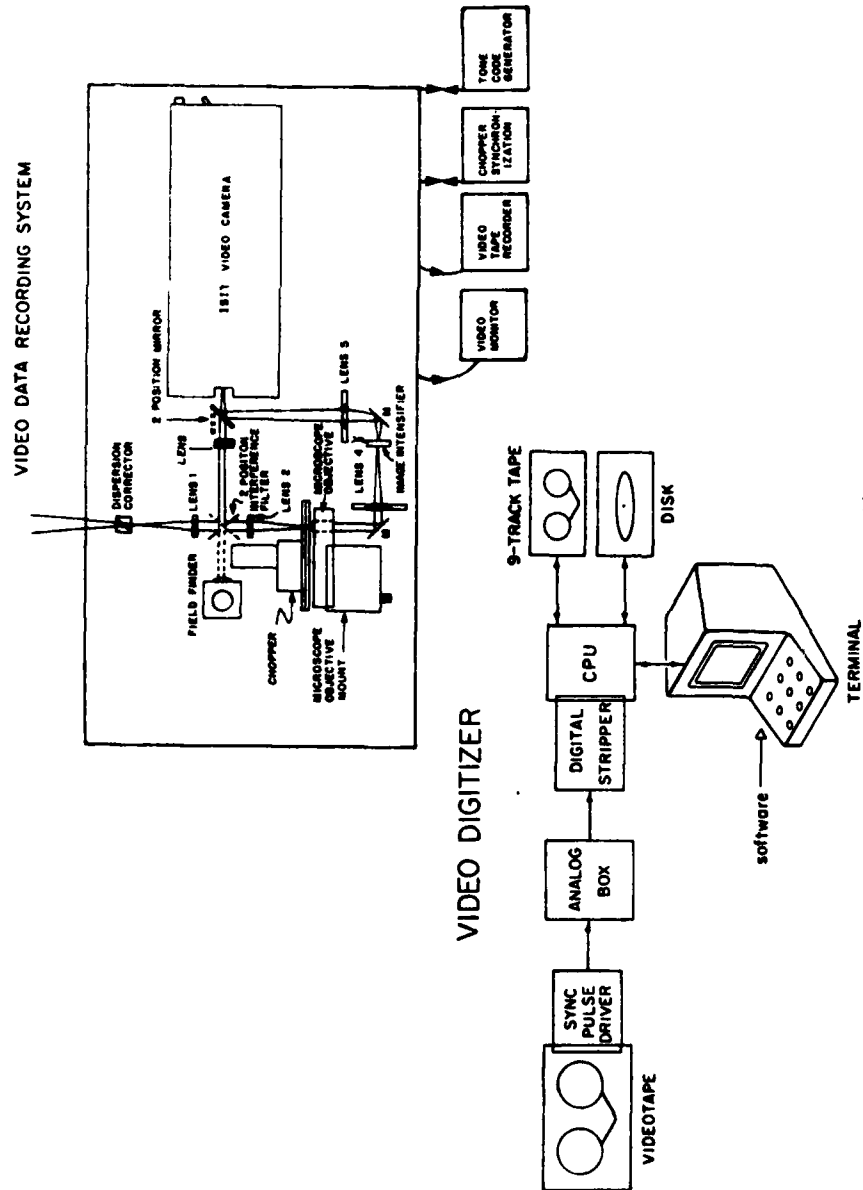


Fig. 2

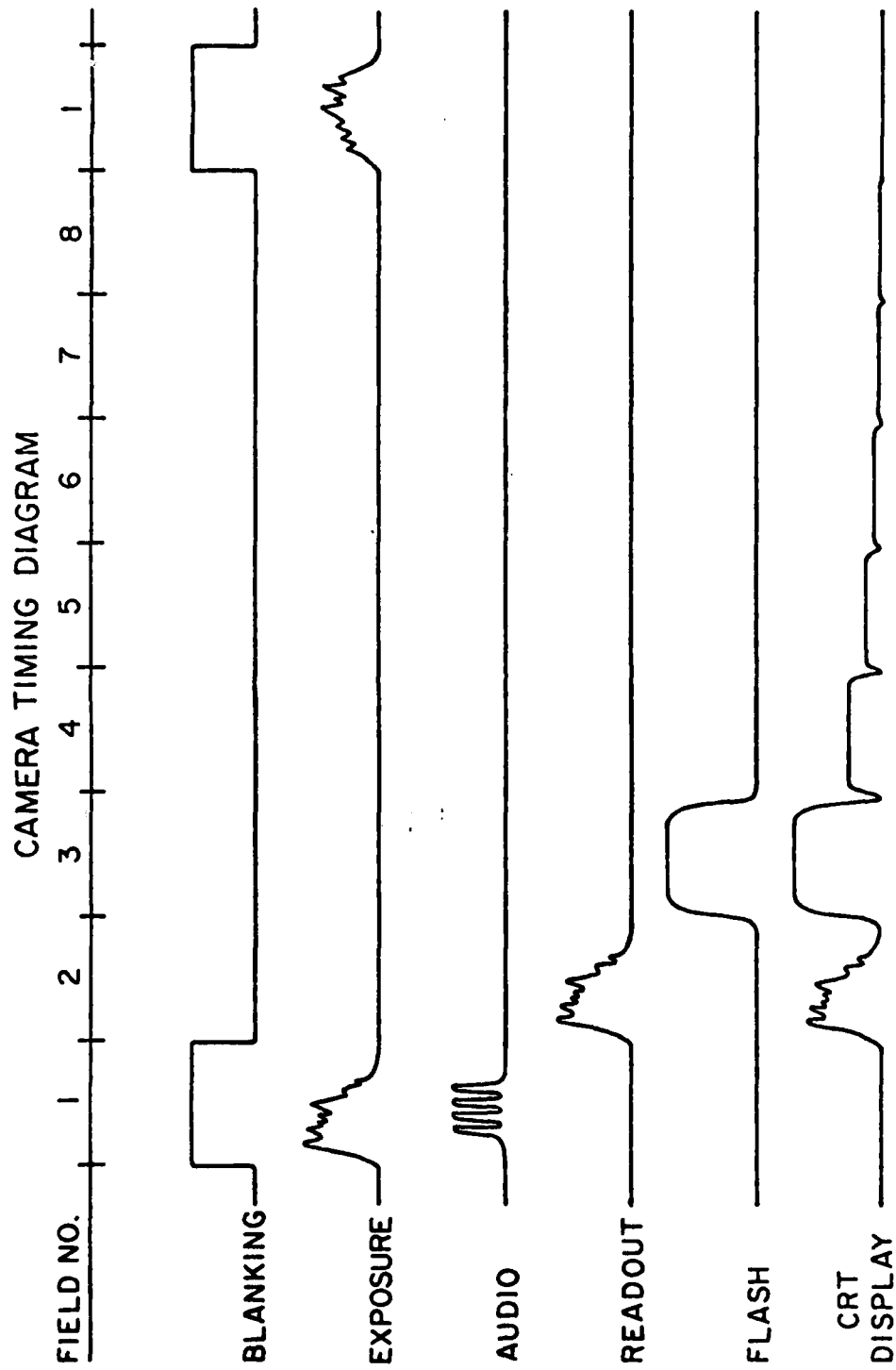


Fig. 3

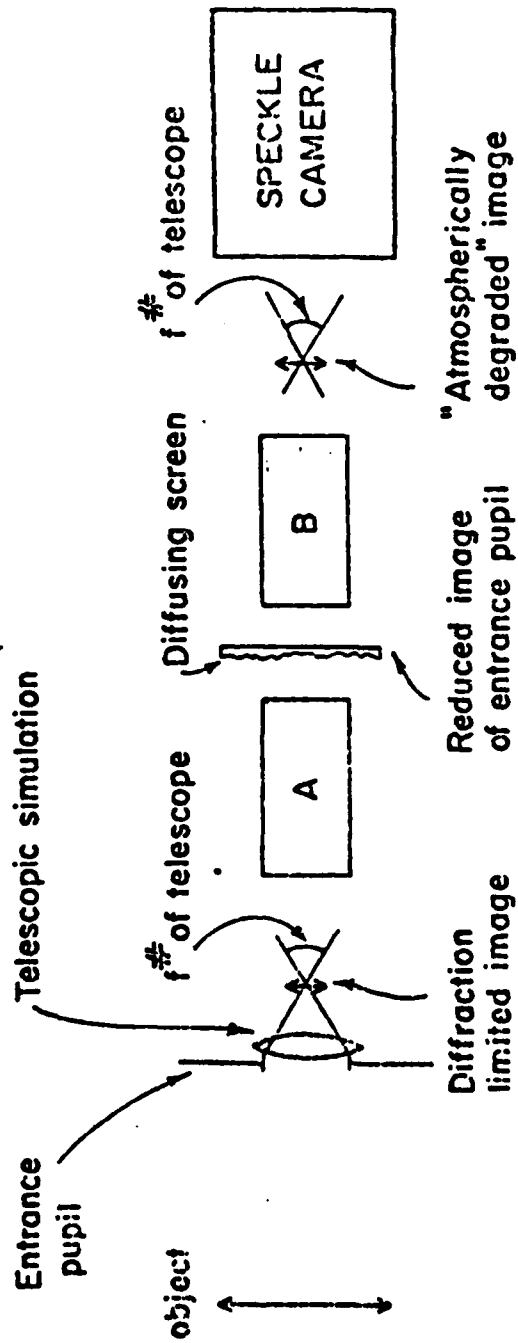
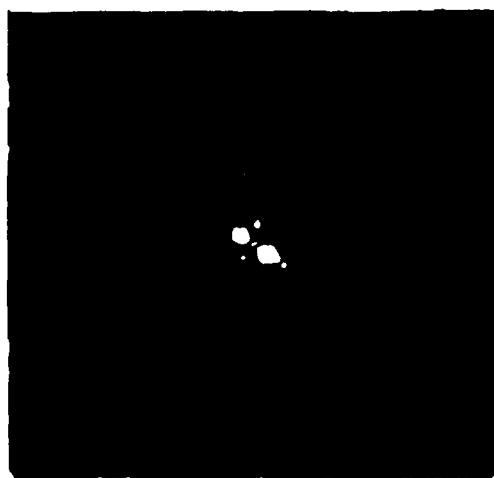


Fig. 4 OPTICAL DIAGRAM OF LABORATORY SPECKLE SIMULATION



c

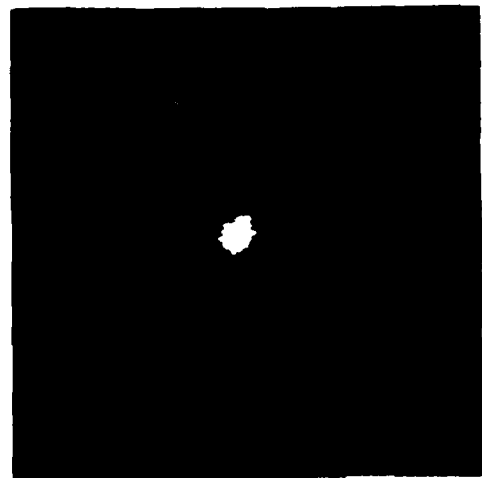


b

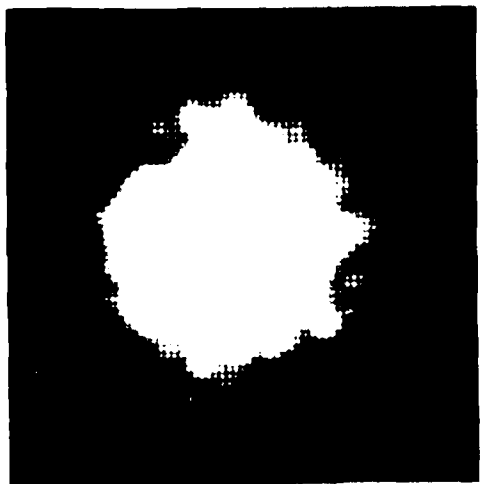


a

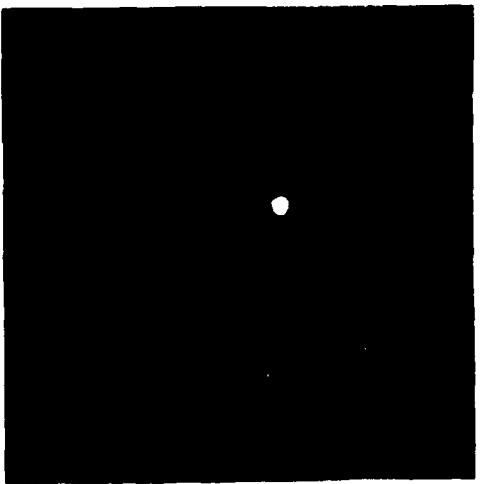
Fig. 5



a



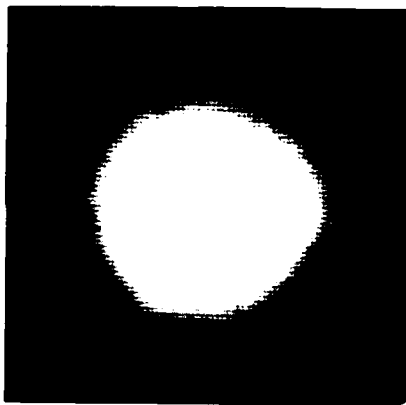
b



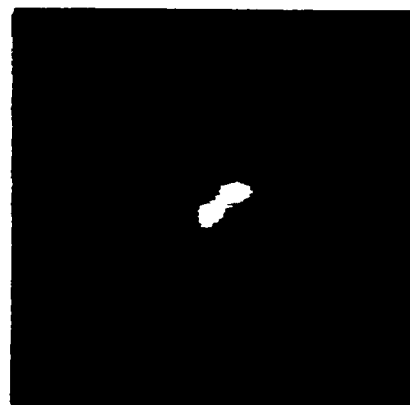
c

Fig. 6

ADS 11640 A



a.

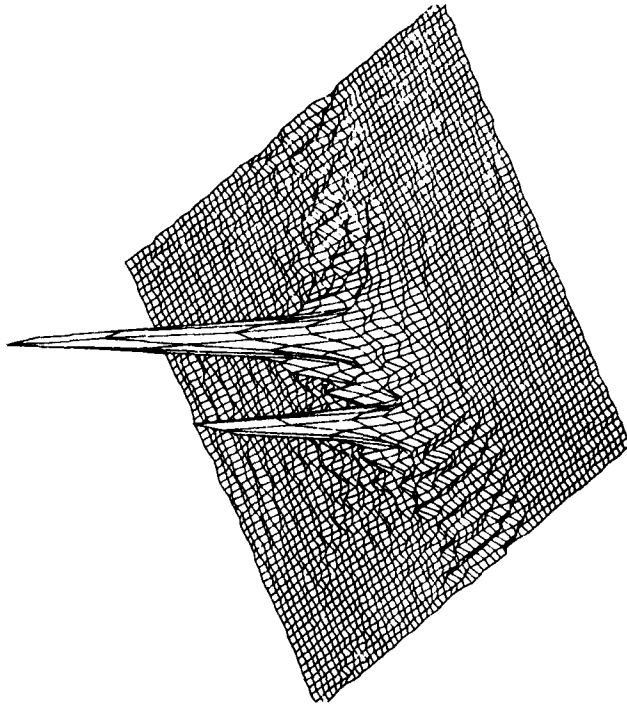


b.

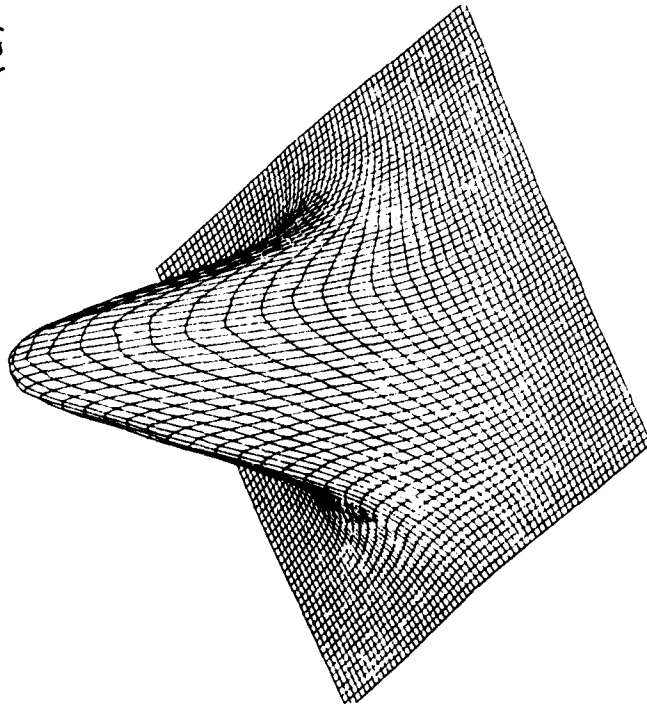


Fig. 7

(b)



(a)



ADSI4073

Fig. 8

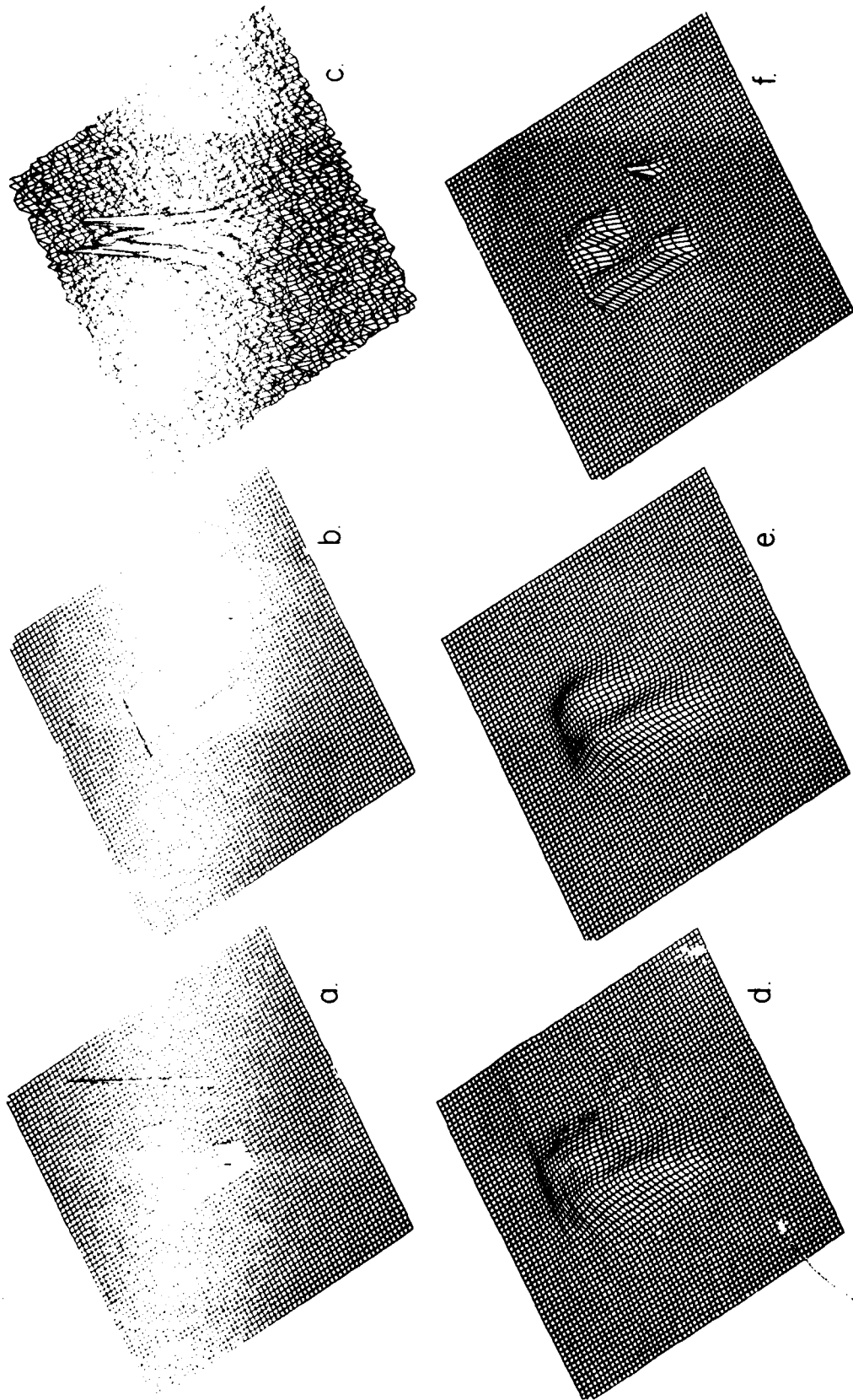
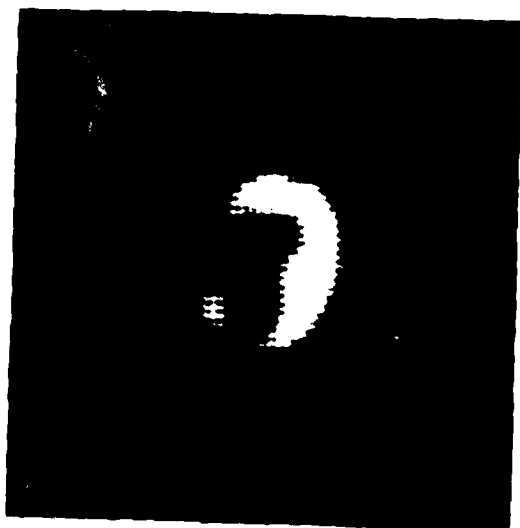
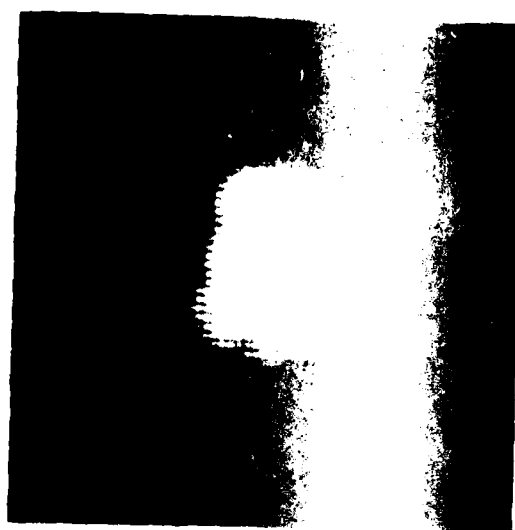


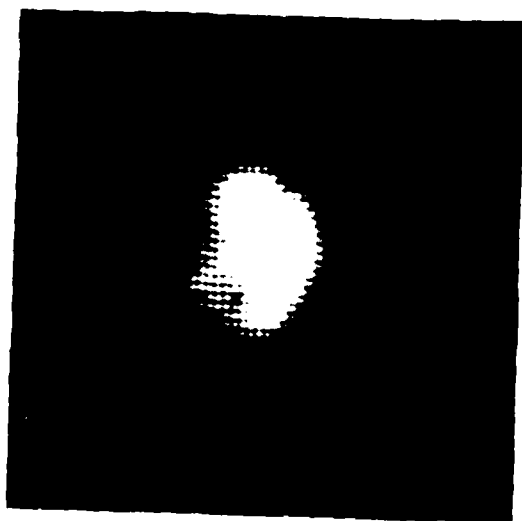
Fig. 9



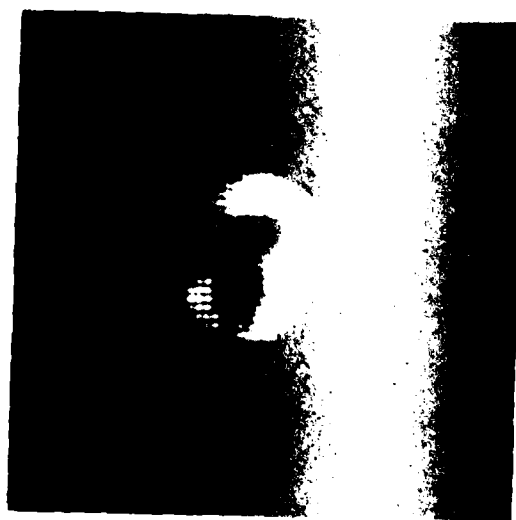
a.



b.

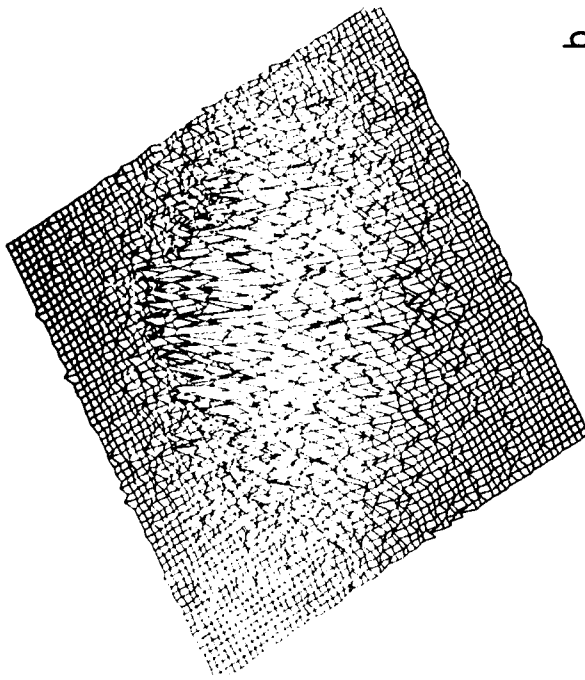


c.

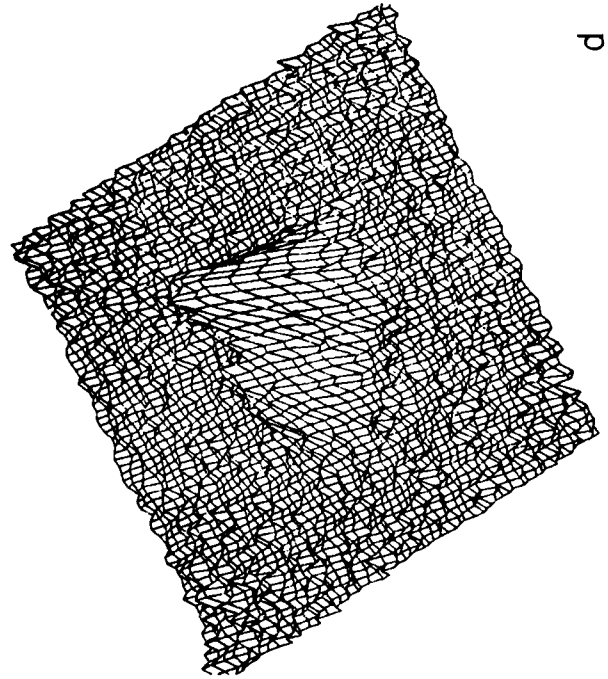


d.

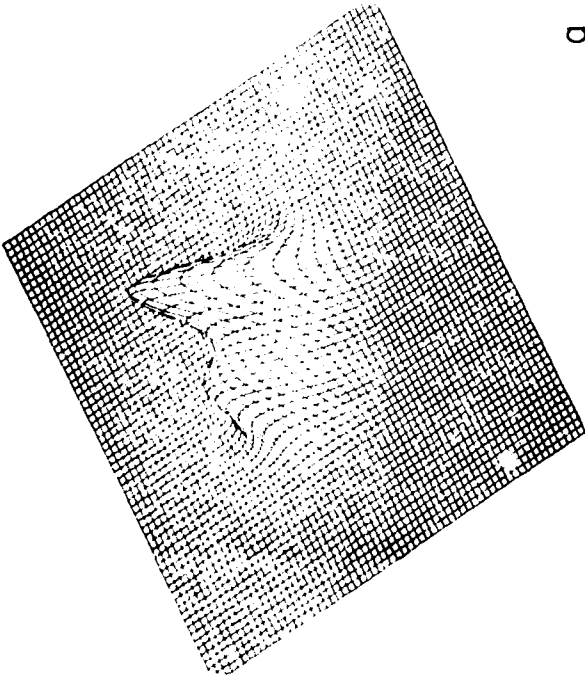
Fig. 10



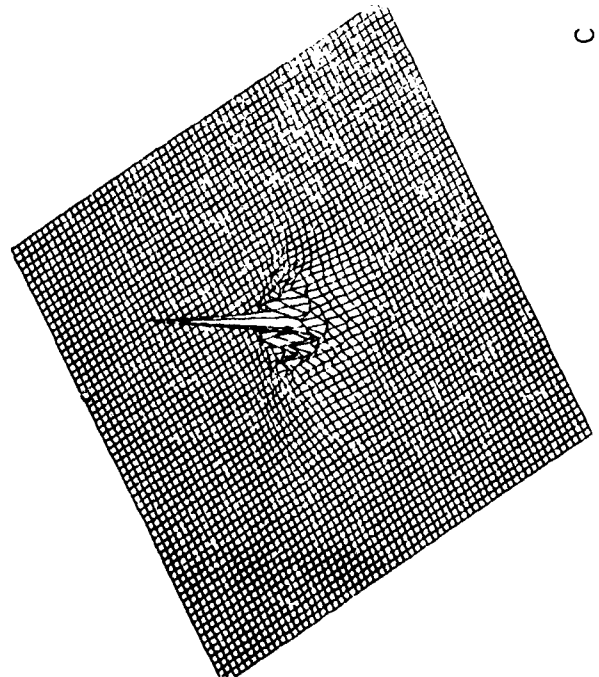
b



d

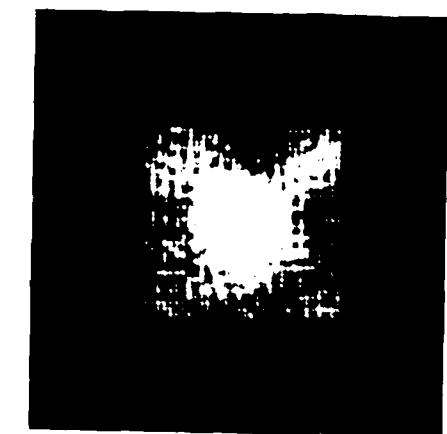


a

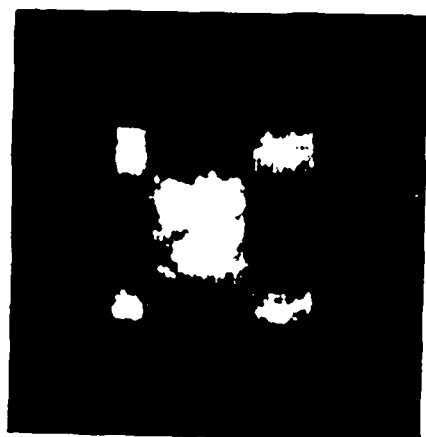


c

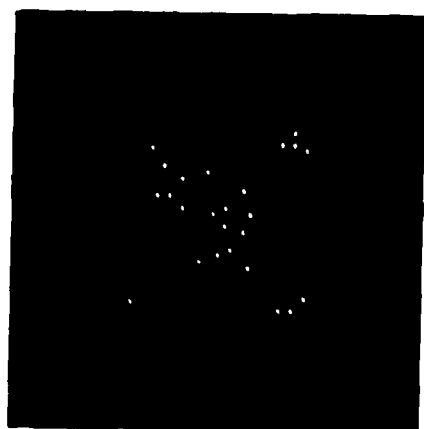
Fig. 11



c.



b.



a.

Figure 12.

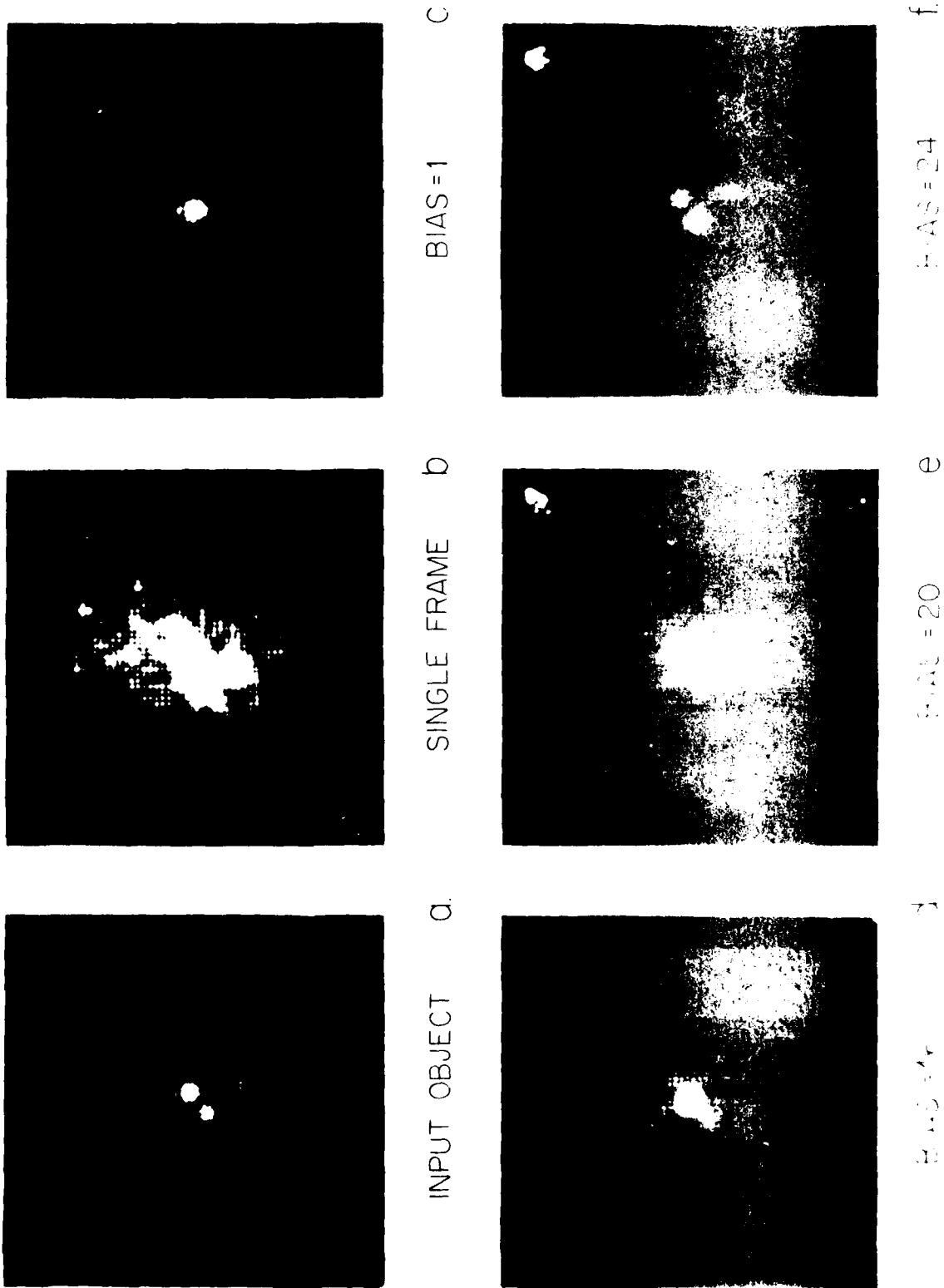


Figure 13.

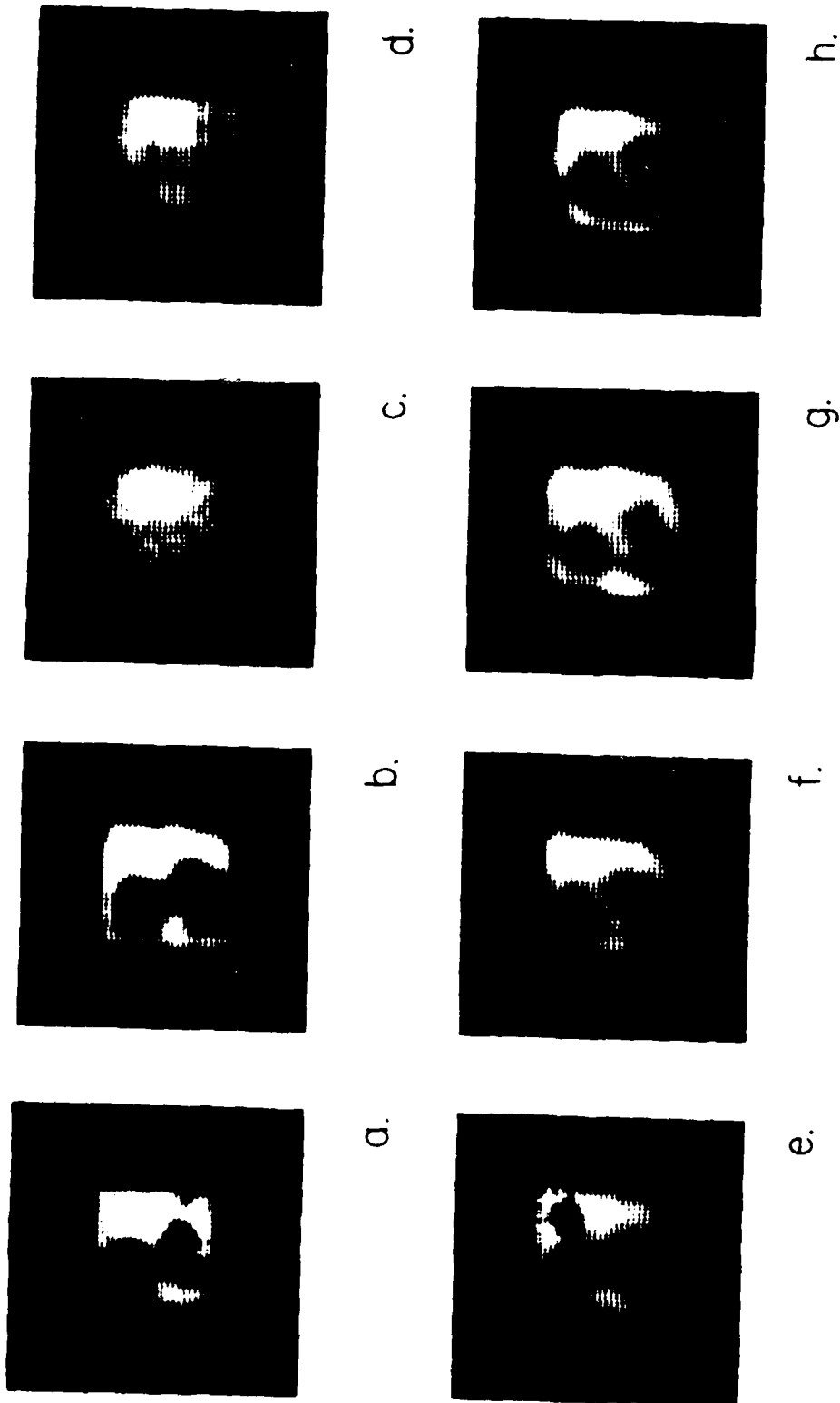
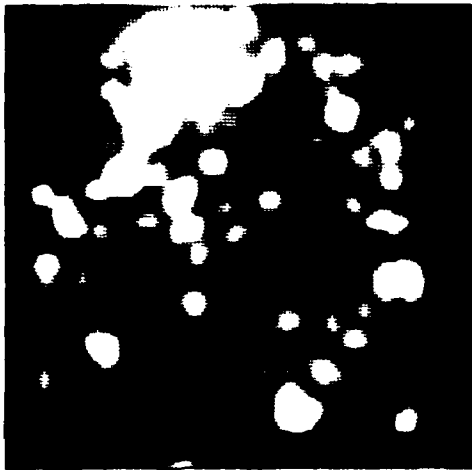


Fig. 14



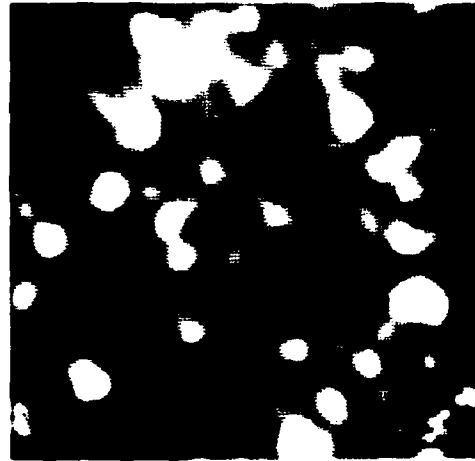
a.



b.



c.



d.

Fig. 15

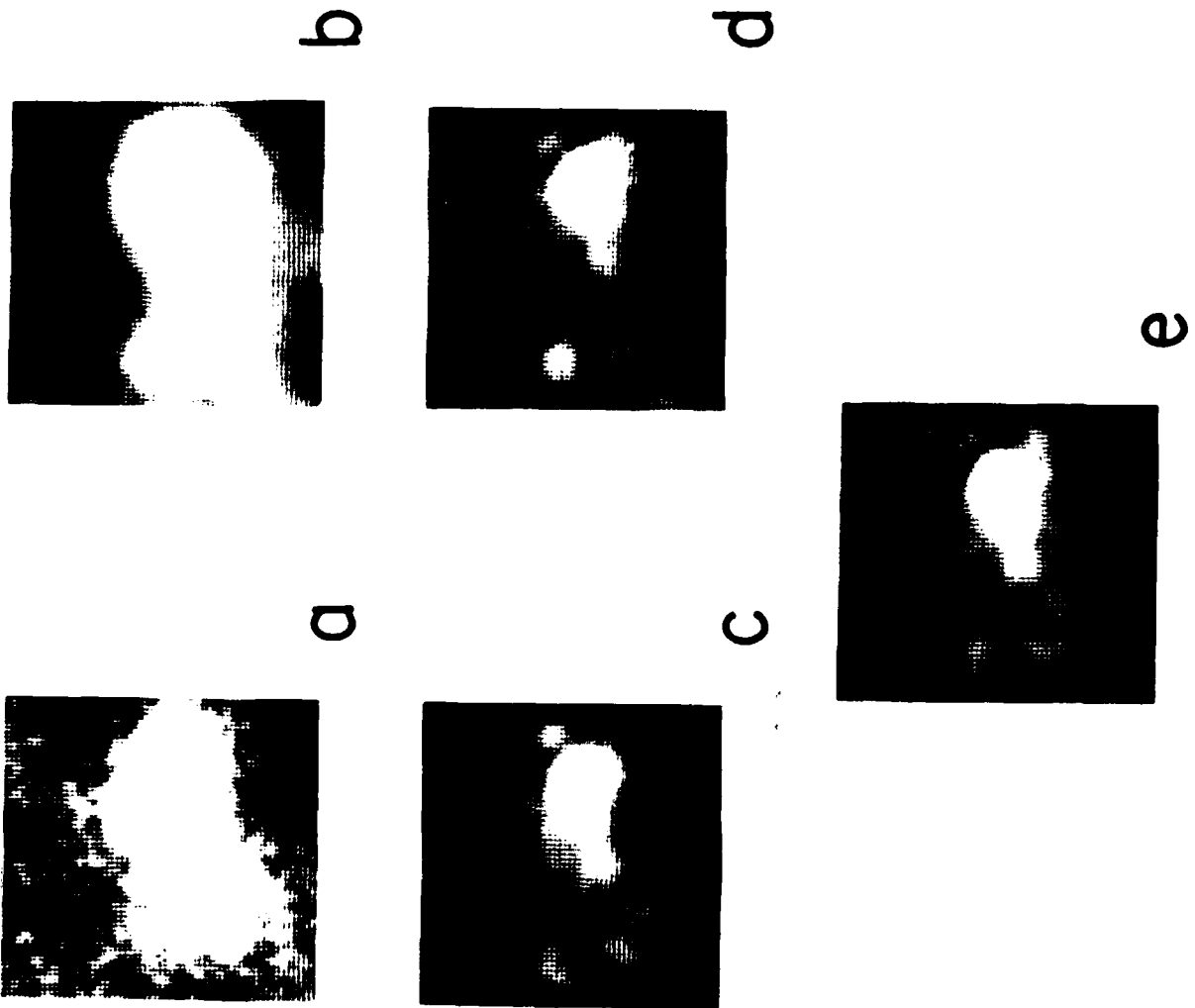


Fig. 16

END

DATE
FILMED

1-82

DTIC